

Improved Synthetic Aperture Focusing Technique with Applications in High-Frequency Ultrasound Imaging

Meng-Lin Li, *Student Member, IEEE*, Wei-Jung Guan, and Pai-Chi Li, *Senior Member, IEEE*

Abstract—Synthetic aperture focusing using a virtual source was used previously to increase the penetration and to extend the depth of focus in high-frequency ultrasonic imaging. However, the performance of synthetic aperture focusing is limited by its high sidelobes. In this paper, an adaptive weighting technique based on a focusing-quality index is introduced to suppress the sidelobes. The focusing-quality index is derived from the spatial spectrum of the scan-line data along the mechanical scan direction (i.e., the synthetic aperture direction) after focusing delays relative to the virtual source have been applied. The proposed technique is of particular value in high-frequency ultrasound in which dynamic focusing using array transducers is not yet possible. Experimental ultrasound data from a 50-MHz imaging system with a single-crystal transducer (f -number = 2) are used to demonstrate the efficacy of the proposed technique on both wire targets and speckle-generating objects. An in vivo experiment also is performed on a mouse to further demonstrate the effectiveness. Both 50-MHz fundamental imaging and 50-MHz tissue harmonic imaging are tested. The results clearly demonstrate the effectiveness in sidelobe reduction and background-noise suppression for both imaging modes. The principles, experimental results, and implementation issues of the new technique are described in this paper.

I. INTRODUCTION

ULTRASONIC imaging in the 2–15 MHz range is used routinely in clinical settings. However, the spatial resolution of conventional ultrasonic imaging systems is inadequate in certain applications. Because resolution improves with the increasing center frequency and the increasing bandwidth, specialized high-frequency ultrasonic imaging systems have been developed recently for the imaging of small-scale superficial structures such as the skin, the anterior chamber of the eye, and mouse embryos [1]–[7].

High-frequency ultrasound has shown promise for clinical use, but several limitations exist. The major problem in high-frequency imaging is tissue attenuation limiting the penetration and reducing the signal-to-noise ratio (SNR). In addition, high-frequency array transducers are still under development; hence, a mechanically scanned, single-crystal transducer with a fixed focus typically is used. Con-

sequently, the image quality is significantly deteriorated in the out-of-focus region [8]–[11].

To improve the image quality of a fixed-focus imaging system, Passman and Ermert [8], [9] proposed a synthetic aperture focusing technique (SAFT) with a virtual source element. The technique increases the penetration and extends the limited depth of focus of a strongly focused transducer; in their case a depth-independent resolution was achieved. Synthetic aperture processing treats the transducer's geometric focus as a virtual source that is assumed to produce an approximately spherical wavefront over a limited angular extent. The fixed-focus, single-crystal transducer is mechanically scanned to acquire a line of data at each scan position. Then, the SAFT is performed by appropriately delaying and summing the scan lines using the virtual-source concept. Frazier and O'Brien [10] examined the tradeoffs between system complexity, grating lobes, and the SNR of the synthesized image in SAFT. Because the sidelobe level of SAFT is high, apodization was applied to reduce sidelobes and to improve contrast resolution [10], [11]. The tradeoff between lateral resolution and sidelobe level with apodization also was studied.

For array beam formation, several methods have been proposed for sidelobe reduction and contrast enhancement. Krishnan *et al.* [12] proposed a Fourier-transform-based adaptive sidelobe-reduction technique, called PARCA2. PARCA2 estimates the unwanted sidelobe contribution from the parallel receive beams reconstructed by Fourier transforming the received channel data along the array direction, then reduces such contribution in the receive signal [12], [13]. However, PARCA2 needs iterations to find the best estimates. Rigby [14] proposed a data-dependent weighting technique using the coherence factor (CF) to increase the contrast resolution. The CF is a focusing-quality index and is used as a weighting factor to the reconstructed image [14], [15]. However, the variation of the CF is large. With the CF weighting, such a variation significantly increases speckle variance in a uniform speckle area, and it may cause image artifacts. Li and Li [16], [17] generalized the coherence factor to cover objects with diffuse scatterers and proposed an adaptive weighting technique based on the generalized coherence factor (GCF) to reduce the focusing errors resulting from the sound-velocity inhomogeneities. The GCF has a smaller variation than the CF. Hence, the GCF weighting is more suitable, particularly for imaging a speckle-generating target. Moreover, the GCF technique rivals PARCA2 in imaging per-

Manuscript received November 27, 2002; accepted September 1, 2003. Support from the National Science Council under grant # NSC 92-2213-E-002-019 is greatly appreciated.

The authors are with the National Taiwan University, Department of Electrical Engineering, Taipei, Taiwan.

P.-C. Li is also with the National Health Research Institutes, Medical Engineering Division, Taipei, Taiwan (paichi@cc.ee.ntu.edu.tw).

formance, but its computational complexity and memory requirements are lower, and no iterations are needed.

In this paper, the GCF weighting technique previously developed for array beamforming is extended to SAFT. The adaptive weighting is based on a focusing-quality index, similar to the GCF described in [16], [17]; here it is used to reduce the sidelobes of SAFT. The focusing-quality index of SAFT is derived from the spatial spectrum of the scan-line data along the scan direction (i.e., the synthetic aperture direction) after appropriate focusing delays have been applied. Experimental ultrasound data was acquired using a 50-MHz ultrasonic imaging system and a single-element transducer with a modest focus (f -number = 2). The efficacy of the proposed technique on both wire targets and diffuse scatterers is tested. The effects on contrast resolution and the background noise level also are explored.

The paper is organized as follows. The SAFT that uses a virtual source is reviewed in Section II. The spatial spectral characteristics of the delayed data acquired by the scanned transducer are explored, and the proposed adaptive weighting approach is introduced in Section III. In Section IV, 50-MHz experimental ultrasound data are used to evaluate the performance of the adaptive weighting technique, concentrating on sidelobe reduction in SAFT images. The technique also is tested on 50-MHz tissue harmonic imaging and in vivo imaging of a mouse in Section IV. The paper concludes in Section V.

II. REVIEW OF THE SAFT WITH A VIRTUAL SOURCE

The SAFT used in this paper treats the transducer's focal point as a virtual source, as shown in Fig. 1(a). The virtual source is assumed to produce a wave propagating both forward and backward with respect to itself that is spherical within a certain angular extent. If a linear scan is performed with the transducer, the sound field generated by the virtual source at the current position will overlap with the sound fields produced at adjacent positions. Hence, synthetic aperture focusing can be performed in the overlapping region before and after the virtual source. As an example, the points p_1 and p_2 in Fig. 1(a) are in the overlapping region after and before the virtual source, and they can be synthetically focused using the received scan lines at which the points p_1 and p_2 are illuminated by the sound field [10], [18].

Fig. 1(b) further illustrates the virtual-source concept. The scan line i is a distance x_i away from the axis of the synthesized beam. The sound field of scan line i propagates through the desired focal point p . Hence, the echo signal from scan line i can be added to the beam constructively by applying an appropriate time delay. Based on the virtual-source concept, the time delay applied to the received signal of scan line i is expressed as:

$$\Delta t_i = 2 \cdot \text{sgn}(z - z_f) \cdot \frac{(r' - r)}{c}, \quad (1)$$

where z is the depth of the synthetic focal point p , z_f is the transducer's focal depth, $r = \text{abs}(z - z_f)$ is the axial

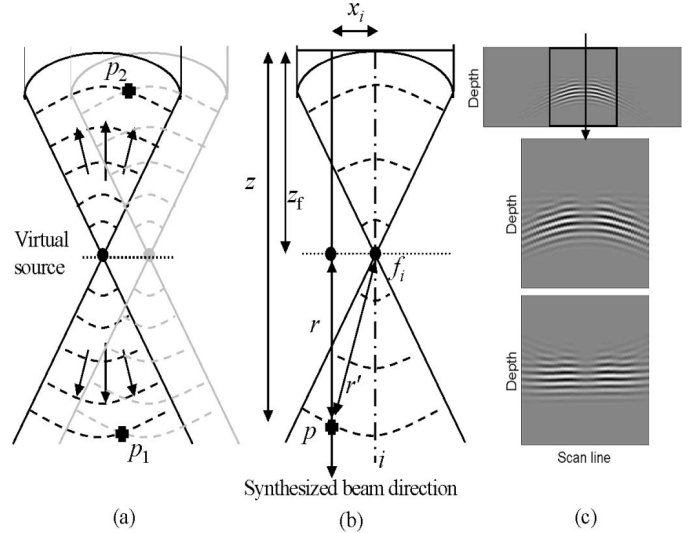


Fig. 1. (a) Schematic of the virtual-source concept. (b) Focusing geometry for the SAFT with a virtual source, where z is the depth of the synthetic focal point p , z_f is the transducer's focal depth, r is the axial distance from the transducer's focal depth to the synthetic focal depth, r' is the distance from the virtual source f_i to the synthetic focal point p . (c) Illustration of the SAFT procedure. In each panel the lateral axis is the scan-line index, and the vertical axis represents the depth. The top panel shows all the simulated RF scan lines for a point beyond the focal depth. The scan lines in the black rectangular box are used to synthesize the beam with a direction denoted by the arrow. The middle panel is the magnified version of the scan-line data in the black rectangular box shown in the top panel. The bottom panel shows the delayed version of the middle panel.

distance from the transducer's focal depth to the synthetic focal depth, $r' = \sqrt{r^2 + x_i^2}$ is the distance from the virtual source f_i to the synthetic focal point, c is the speed of sound, and $\text{sgn}(\cdot)$ is the signum function. Note that, if the synthetic focal point is located in front of the transducer's focal point, the time delay is negative. After appropriate delays relative to the virtual source are applied to all corresponding scan lines according to (1), SAFT is implemented as the following sum:

$$S_{\text{SAFT}}(t) = \sum_{i=0}^{N-1} S(i, t - \Delta t_i), \quad (2)$$

where $S(i, t)$ is the received signal at the scan line i . The maximum number of scan lines included in the sum of (2) is denoted by N and is determined by the angular extent of the virtual-source sound field [8]–[10], where a wider angular extent allows more scan lines to contribute to the sum. Hence, a more tightly focused beam can be synthesized after SAFT is applied as the effective aperture size is increased. Note that around the focal point of the transducer, the number of scan lines that can contribute to focusing is limited. Such a drastic change in the number of available scan lines causes discontinuity in the SAFT image, which can be reduced by applying appropriate gain compensation [18].

The procedures of the SAFT are further illustrated in Fig. 1(c), in which the horizontal axis of each panel is

the scan-line index and the vertical axis represents the depth. The top panel shows all the simulated radio frequency (RF) scan lines for a point beyond the focal depth, with the transducer being linearly scanned. Each line represents the RF A-scan data at that position, and the entire panel represents the unfocused beam profile. As an example, the scan lines in the black rectangular box are used to synthesize the beam with a direction denoted by the arrow (the scan lines in this region are magnified in the middle panel). The number of scan lines in the black box is determined by the angular extent of the virtual-source sound field [10]. The bottom panel presents the delayed version of data shown in the middle panel, demonstrating that all the scan lines are aligned after the delays are applied. Summing the delayed scan lines along the horizontal axis produces a beam with a synthetic focus. Note that the delayed scan lines are not identical, with the amplitude variations corresponding to the unfocused beam profile at that depth. This is different from received array channel data, in which the radiation pattern of each individual channel is more uniform. In addition, a baseband SAFT is implemented in this paper to reduce the data sampling requirements associated with a high-frequency system [19].

III. THE ADAPTIVE WEIGHTING TECHNIQUE

In this section, the GCF weighting technique previously proposed for array beam formation is extended to SAFT [16], [17]. For SAFT with a virtual source, the weighting factor is derived from the spatial spectrum of the delayed scan-line data, which is the data received by the single-element transducer at each scan position after the focusing delays of the corresponding virtual source are applied prior to beam summation. The N -point discrete Fourier spectrum of the delayed scan-line data along the primary scan direction can be expressed as:

$$p(k, t) = \sum_{i=0}^{N-1} S_{\text{delayed}}(i, t) e^{-j2\pi \frac{ik}{N}}, \quad (3)$$

$$k = -N/2, -N/2 + 1, \dots, N/2 - 1,$$

where $S_{\text{delayed}}(i, t)$ is the delayed signal of scan line i , N is the total number of scan lines included in the sum of (2), and k is the spatial frequency index. Note that, if baseband scan-line data is used, the Fourier spectrum along the scan direction can be viewed as the approximation of the two-way radiation pattern (i.e., transmit and receive) centered on the direction of the synthesized beam [12], [13]. The direct current (DC) component [i.e., $p(0, t) = \sum_{i=0}^{N-1} S_{\text{delayed}}(i, t)$] represents the beam sum of the delayed scan-line data, and it corresponds to the signal from the direction of the synthesized beam direction, i.e., the main lobe. The high-frequency components correspond to the scattered signals from other angles, i.e., the sidelobes, when baseband scan-line data is used.

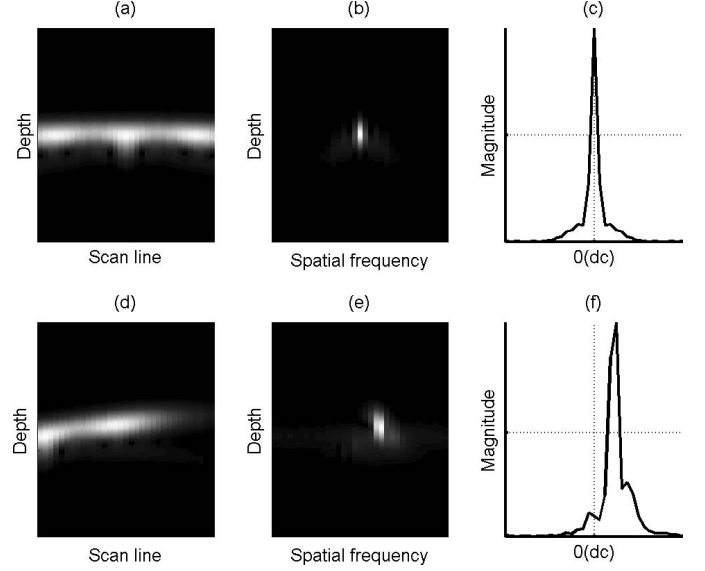


Fig. 2. Delayed baseband scan-line data and the associated spectra along the scan direction for a point target. The top panels are for the case with a wire in the direction of the synthesized beam, located 1.2 mm in front of the focal point. The bottom panels show the case in which the wire is off the synthesized beam axis. In each case, the left column [(a) and (d)] shows the amplitude of the delayed baseband scan-line data, with the horizontal axis representing the scan-line index and the vertical axis denoting the depth; the middle column [(b) and (e)] shows the spectrum at each depth. The right column [(c) and (f)] is the projection of the data shown in the middle column.

Fig. 2 shows simulated baseband scan-line data and the associated spectra along the scan direction. A single-crystal transducer with a diameter of 6 mm and a geometric focus at 12 mm was simulated. The simulated transducer's center frequency was 50 MHz of 55% -6 dB fractional bandwidth. The transmit signal was a Gaussian pulse with a center frequency of 50 MHz. The spacing between two adjacent scan lines was $10 \mu\text{m}$. The top panels in Fig. 2 present the case in which a point target was in the direction of the synthesized beam, located 1.2 mm in front of the focal point. Fig. 2(a) shows the amplitude of the delayed baseband scan lines, in which the vertical axis is the depth and the horizontal axis is the scan direction. It can be seen that the scan lines are generally in phase (i.e., horizontal wavefront), but the amplitude variations are large as the point target was illuminated by an unfocused beam. Fig. 2(b) shows the corresponding one-dimensional Fourier transform of the delayed scan lines along the scan direction at each range, with the horizontal axis representing the spatial frequency index k from $-N/2$ to $N/2 - 1$. Fig. 2(c) is the projected spectrum of Fig. 2(b), and the vertical dotted line indicates DC (i.e., the direction of the synthesized beam). The maximum along the depth direction is used for the projection. Though the data along the scan direction exhibit amplitude variations, the spectrum energy is primarily concentrated in the low-frequency region near DC (i.e., the direction of the synthesized beam).

The bottom panels of Fig. 2 show the case in which the point target was off the synthesized beam axis, with

the other conditions unchanged. In other words, this corresponds to a steering error of SAFT. Fig. 2(d) shows that the delayed data are no longer in phase, with the slope of the (tilted) wavefront corresponding to the direction of the point target. In other words, the scan-line data at each range are modulated. Hence, the corresponding spectrum energy along the scan direction is generally concentrated in the object direction instead of in the direction of the synthesized beam, as shown in Figs. 2(e) and (f). A significant portion of the spectrum energy is distributed in the higher frequency region of the spectrum (i.e., away from the direction of the synthesized beam). In this case, the contribution of the off-axis target to the primary beam direction needs to be minimized.

The simulated data in Fig. 2 shows that the spectrum of the scan-line data can be used to approximate the radiation pattern and to determine the focusing quality of SAFT. The focusing quality of SAFT is directly related to the ratio of the energy in the low-frequency region (around DC) to the total energy (i.e., the ratio of the energy received from angles near the direction of the synthesized beam to the total energy from all directions if baseband scan-line data is used). Hence, such an energy ratio (ER) can be used as a focusing-quality index for SAFT, and it is similar to the generalized coherence factor as described in [16], [17]. According to the parameters defined in (3), the ER at a given depth can be expressed as:

$$\text{ER}(t) = \frac{\text{energy in the low-frequency region}}{\text{total energy}} = \frac{\sum_{k=-M_0}^{M_0} |p(k, t)|^2}{\sum_{k=-N/2}^{N/2-1} |p(k, t)|^2}. \quad (4)$$

The discrete Fourier transform can be efficiently computed using the fast Fourier transform (FFT). The low-frequency region is specified by a cutoff frequency M_0 in the spatial frequency index. The procedure of ER calculation is illustrated in Fig. 3(a). Note that an M_0 of zero means that the low-frequency range used to estimate ER is restricted to DC only. However, because a speckle-generating target inherently contains a certain degree of incoherence, with diffuse scatterers the cutoff frequency M_0 should be large enough to allow for this [16], [17].

A high ER indicates that the image object is in the direction of the synthesized beam, and thus the image intensity should be maintained. However, a low ER should be used to reduce the contribution of sidelobes from the outside objects to the image intensity. Hence, SAFT image quality can be improved by developing an adaptive weighting technique based on this property. The ER-weighted signal $S_{\text{weighted}}(t)$ of the SAFT signal $S_{\text{SAFT}}(t)$ at a given range can be expressed as:

$$S_{\text{weighted}}(t) = \text{ER}(t) \cdot S_{\text{SAFT}}(t). \quad (5)$$

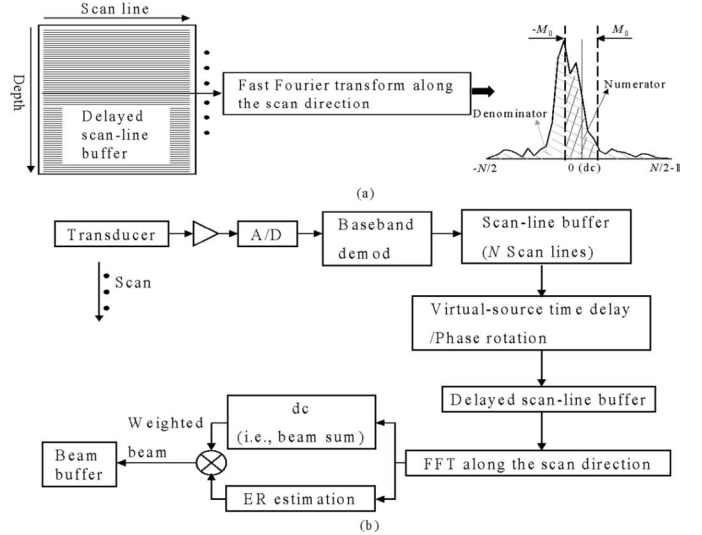


Fig. 3. (a) Schematic showing how the ER is calculated. (b) System block diagram of the adaptive weighting technique for SAFT.

Note that, for each beam, the weighting needs to be calculated and applied at each imaging depth. The weighting is calculated for each individual SAFT image. A system block diagram of the adaptive weighting technique for SAFT is shown in Fig. 3(b). As described previously, one reason for implementing the SAFT in baseband is to reduce the large data sampling rate associated with a high-frequency system. The transducer is linearly translated along the scan direction during data acquisition. The echo signal at each scan position is received and digitized by an analog-to-digital converter, then the received RF data are demodulated down to baseband and stored in the scan-line buffer. After N scan lines are collected, appropriate virtual-source time delays and phase rotations are applied before the data are sent to the delayed scan-line buffer. The ER then is estimated using the FFT of the delayed baseband scan-line data (note that ER should be calculated at all depth points). The DC component of the spectrum (i.e., the beam sum) is then weighted by the ER, by multiplying the amplitude of the beam sum data by the corresponding ER on a point-by-point basis. The weighted data then are sent to the beam buffer for further signal processing and display [17].

IV. EXPERIMENTAL RESULTS

Experiments were conducted to investigate the efficacy of the adaptive weighting technique on sidelobe reduction in SAFT imaging. A lithium-niobate focused transducer (NIH Resource Center for Medical Ultrasonic Transducer Technology, Penn State University, University Park, PA) was used. The transducer's center frequency is 45 MHz of 55% -6 dB fractional bandwidth. The transducer has a diameter of 6 mm and is geometrically focused at 12 mm. A diagram of the experimental setup is shown in Fig. 4. An arbitrary-function generator (Signatec DAC200, Corona,

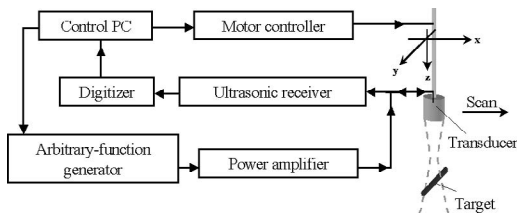


Fig. 4. Diagram of the experimental setup.

CA) was used to generate the desired transmit waveform, which then was sent to a power amplifier (Amplifier Research 25A250A, Souderton, PA) to drive the lithium-niobate focused transducer. A three-axis motor system (CSIM, Taipei, Taiwan) was used to control the relative position between the target and the transducer. The transducer was stepped laterally, and the scan-line data acquired at each position were sent to an ultrasonic receiver (Panametrics 5900, Waltham, MA). Finally, the signal was sampled with an analog-to-digital converter operating at 500 Msamples/s and 8-bit resolution (Signatec PDA500).

For 50-MHz fundamental imaging, a Gaussian pulse with a center frequency of 50 MHz was transmitted. For 50-MHz second harmonic imaging, a Gaussian pulse at 25 MHz was used such that the second harmonic signal at 50 MHz can be obtained at an adequate SNR in our high-frequency imaging system. In addition, for in vivo mouse imaging, a Gaussian pulse at 25 MHz was also used in order to obtain better penetration and a higher SNR. The spacing between two adjacent scan lines was $10\text{ }\mu\text{m}$ for phantom imaging and $20\text{ }\mu\text{m}$ for 25-MHz in vivo mouse imaging, both of which were smaller than half wavelength at the imaging frequency of the two imaging formats to reduce the grating lobe [10]. The maximum number of scan lines for beam synthesis was limited to 32 for all the following cases, although the actual number of available scan lines may have been larger. This limitation reduced the implementation complexity of SAFT and sped up the ER calculation. The sound velocity was assumed to be $1.48\text{ mm}/\mu\text{s}$. The depths of the imaged targets were estimated using the assumed sound velocity. In addition, $M_0 = 1$ and $M_0 = 3$ were used to calculate the ER for wire targets and speckle-generating targets, respectively. All images were displayed with a 55-dB dynamic range.

A. Wire Target

The wire target comprised a nylon wire with a diameter of 52 μm . Fig. 5 shows the results when the wire target was located at a depth of 12.6 mm, which was 0.6 mm beyond the focal depth. Figs. 5(a)–(c) show the original, SAFT, and SAFT-plus-weighting images, respectively, where the vertical axis is the depth and the horizontal axis is the lateral position, both in millimeters. Although SAFT improves the image quality over the original image, the side-lobe level of the SAFT image is still high. This high side-lobe level is noticeably suppressed by the adaptive weighting technique, as shown in Fig. 5(c). Note that the image

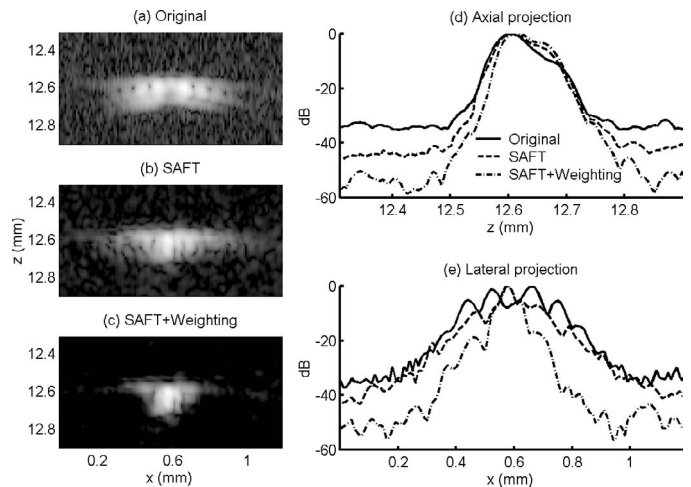


Fig. 5. Experimental results for a wire target located at a depth of about 12.6 mm. (a), (b), and (c) show the original, SAFT, and SAFT-plus-weighting images, respectively, in which the vertical axis is the depth and the horizontal axis is the lateral position, both in millimeters. (d) and (e) show the axial and lateral projections of the images shown in (a), (b), and (c). The solid lines are the original case, the dashed lines are the SAFT case, and the dash-dotted lines are the case after adaptive weighting. The images shown here and in subsequent figures are displayed with a 55-dB dynamic range.

background noise is also reduced after adaptive weighting. Figs. 5(d) and (e) show the axial and lateral projections of the images shown in Figs. 5(a)–(c). The sidelobe level of the SAFT image is suppressed more than 10 dB after weighting. The axial projection shows that the noise floor of the weighted image is about 8 dB lower than that of the SAFT image. Fig. 6 shows the results in which the wire target was located at a depth of 10.76 mm, which was 1.24 mm in front of the focal depth. As in Fig. 5, significant image quality improvement is achieved with adaptive weighting.

B. Anechoic Cyst

A gelatin-based phantom also was constructed and imaged to demonstrate the efficacy of the adaptive weighting technique on improving contrast resolution. The gelatin-based phantom had a 500- μm anechoic region (a cyst) at its center and graphite powder (1–2 μm , Aldrich Chemical, Milwaukee, WI) distributed uniformly in the background. Figs. 7(a)–(c) show the original, SAFT, and SAFT-plus-weighting images, respectively. The center of the cyst was located at a depth of 13.15 mm, which was 1.15 mm beyond the focal depth. The vertical axis is the depth and the horizontal axis is the lateral distance, both in millimeters. Fig. 7 shows that detection of the cyst is noticeably improved after the adaptive weighting technique: the weighted image is less “filled in” in the cyst region than the SAFT image.

The contrast-to-noise ratio (CNR) is used to quantitatively evaluate the improvement in contrast resolution. The CNR is calculated by taking the ratio of the image contrast to the standard deviation of image intensity in

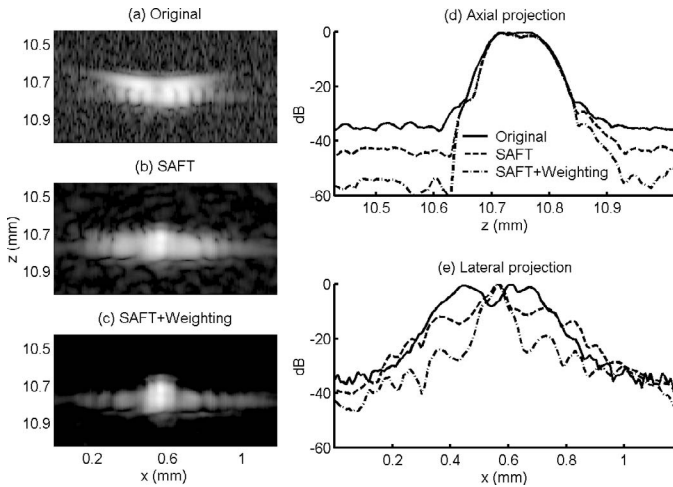


Fig. 6. Experimental results for a wire target located at the depth of 10.76 mm. (a), (b), (c) show the original, SAFT, and SAFT-plus-weighting images, respectively, in which the vertical axis is the depth and the horizontal axis is the lateral position, both in millimeters. (d) and (e) show the axial and lateral projections of the images shown in (a), (b), and (c). The solid lines are the original case, the dashed lines are the SAFT case, and the dash-dotted lines are the case after adaptive weighting.

the background region, where the contrast is defined as the difference (in decibels) between mean intensity values in the background and the cyst region [11]. Note that the background and cyst regions are indicated by the left and right-hand white boxes in Fig. 7(c), respectively. The CNRs are 1.20 for the original image, 2.02 for the SAFT image, and 2.67 for the SAFT-plus-weighting image, which demonstrates that adaptive weighting results in a higher CNR.

C. 50-MHz Second Harmonic Imaging

The effectiveness of the adaptive weighting technique on tissue second harmonic imaging also was tested. In this case, a 25-MHz pulse was used on transmit, and the received second-harmonic signal at 50 MHz was extracted by the pulse-inversion technique, which can reduce harmonic leakage resulting from the transmit waveform and the system nonlinearities [20]–[24]. According to [25], the focal depth of the second-harmonic signal at such high frequencies is close to that of the fundamental signal at the same frequency. Hence, positions of the virtual sources for 50-MHz second-harmonic imaging are assumed to be the same as those for 50-MHz fundamental imaging. The same experimental setup as used for the previous fundamental-frequency experiments was used, along with the same wire target. Fig. 8 shows the harmonic images where the wire target was located 0.69 mm beyond the focal depth. Fig. 8 has the same format and was obtained under the same experimental conditions as Fig. 5. It is clearly shown that the adaptive weighting technique also is effective for tissue harmonic SAFT imaging, with the image background noise also being significantly reduced.

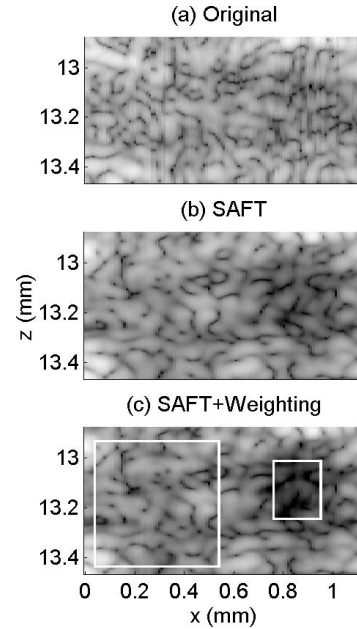


Fig. 7. Images of an anechoic cyst. The vertical axis is the depth, and the horizontal axis represents the lateral position, both in millimeters. (a) Original, (b) SAFT, (c) SAFT plus adaptive weighting. The two white boxes indicate the cyst and the background regions used for CNR calculations.

D. In Vivo Imaging of a Mouse

An in vivo experiment on a mouse (C57BL/6) was also performed. The mouse was purchased from the National Animal Center, Taipei, Taiwan, R.O.C., and was housed in an animal room with good environmental control. Food and water were available ad lib. The use and care of animals were in accordance with the principles of the National Animal Center of the Republic of China.

The mouse was anesthetized with ether during imaging. The lower abdomen and back regions of the anesthetized mouse were wet-shaved to provide a clear window to imaging. Figs. 9(a)–(c) show the corresponding 25-MHz original, SAFT, and SAFT-plus-weighting kidney images, respectively, where the vertical axis is the depth and the horizontal axis is the lateral position, both in millimeters. The imaging depth was from about 6 mm to 14 mm, and the transducer's geometric focal point was at 12 mm. The weighted image in Fig. 9(c) exhibits superior edge definition and sharper contrast than the SAFT image in Fig. 9(b) over the entire depth of imaging field. The image background noise is also suppressed by adaptive weighting. Fig. 9(d) shows the scan-line data along the white dotted vertical lines shown in Figs. 9(a)–(c). In addition to side-lobe reduction, the noise floor in the anechoic region is about 10 dB lower than that without weighting.

V. CONCLUSIONS

The ER in (4) is defined without taking noise into consideration. The relationship between ER without noise

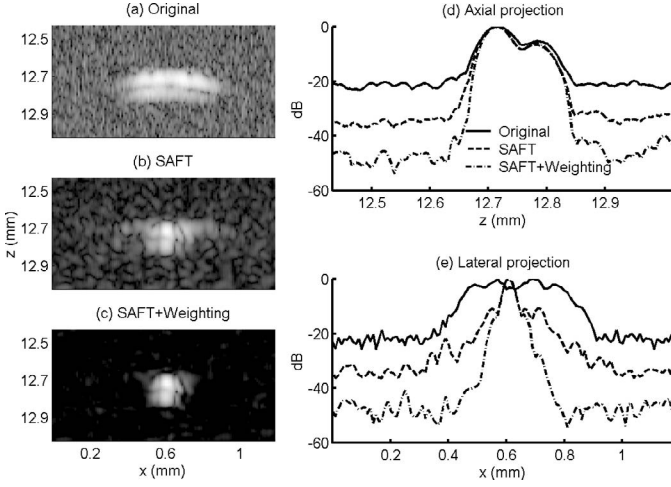


Fig. 8. The 50-MHz second-harmonic experimental results for a wire target located 0.69 mm beyond the focal depth. (a), (b), (c) show the original, SAFT, and SAFT-plus-weighting images, respectively, in which the vertical axis is the depth and the horizontal axis is the lateral position, both in millimeters. (d) and (e) show the axial and lateral projections of the images shown in (a), (b) and (c). The solid lines are the original case, the dashed lines are the SAFT case, and the dash-dotted lines are the SAFT-plus-weighting case.

(i.e., an infinite SNR) and the estimated ER with a finite SNR (denoted by ER') can be expressed as:

$$ER' = \frac{\left(ER \cdot SNR + \frac{2M_0 + 1}{N} \right)}{1 + SNR}, \quad (6)$$

where N is the number of points used for the FFT [17]. If the SNR is much less than one, the ER' can be expressed as:

$$ER' \approx \frac{(2 \cdot M_0 + 1)}{N}. \quad (7)$$

In this case the ER' is about 0.09 (i.e., for $M_0 = 1$ and $N = 32$). Because the SNR in the image background (i.e., the anechoic region) is very low, the image intensity is reduced by applying weighting. Thus, as shown in the experimental results, the adaptive weighting technique effectively suppresses the noise floor in the image background. In addition, as defined in (4), ER fluctuates in a uniform speckle region. When SNR is taken into account, according to (6), fluctuation of ER' will be more serious because SNR varies in a uniform speckle region. Thus, speckle variance in a uniform speckle region may be increased after applying the adaptive weighting technique. To address this problem, the standard deviation of the image intensity is calculated in the background region of the anechoic cyst phantom in Section IV for the three cases: SAFT, SAFT-plus-weighting with $M_0 = 1$, and SAFT-plus-weighting with $M_0 = 3$. The standard deviation of the ER -weighted image with $M_0 = 1$ is 3.5 dB higher than that of the SAFT image, and the standard deviation of the ER -weighted image with $M_0 = 3$ is only 0.54 dB higher than that of the SAFT image. That is, the effect of introducing higher speckle variance after weighting is more

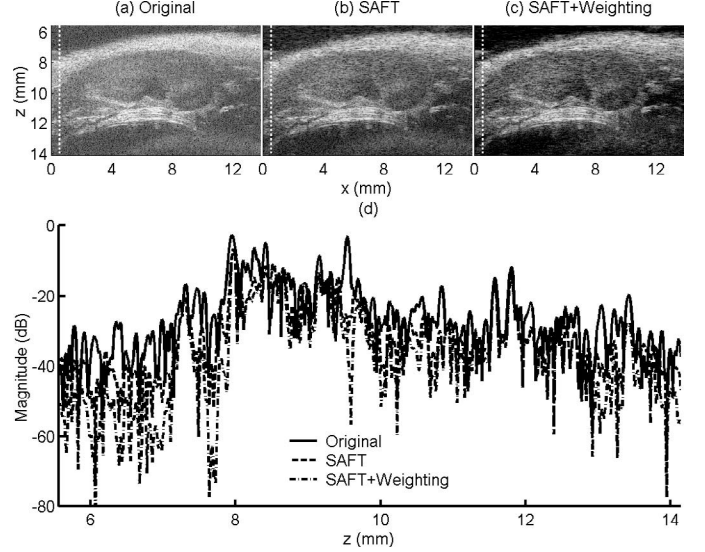


Fig. 9. The 25-MHz in vivo imaging of a mouse kidney. (a), (b), and (c) show the 25-MHz original, SAFT, and SAFT-plus-weighting images, respectively, in which the vertical axis is the depth and the horizontal axis is the lateral position, both in millimeters. (d) shows the scan-line data along the white dotted lines shown in (a), (b), and (c). The solid line is the original case, the dashed line is the SAFT case, and the dash-dotted line is the case after adaptive weighting.

pronounced when a smaller M_0 is used, but it can be reduced with a larger M_0 . Thus, a larger M_0 is generally more preferable for a speckle-generating target [16], [17].

The adaptive weighting technique using the GCF was developed for array beam formation to reduce the focusing errors resulting from sound-velocity inhomogeneities [16], [17]. In this paper, the adaptive weighting technique was extended to reduce the sidelobes of the SAFT radiation pattern, and it was applied successfully to high-frequency ultrasound in which dynamic focusing using arrays is not yet feasible. Experimental results from a 50-MHz imaging system demonstrate the effectiveness of the adaptive weighting technique in both fundamental and tissue harmonic imaging. The sidelobe level was effectively suppressed, and contrast resolution was significantly improved. In addition, the image background noise was lower after the weighting. Although the results are demonstrated only at certain imaging depths, it is expected that the proposed technique can be effectively applied wherever the SAFT is applicable. It is preferable for the proposed technique to be implemented with a baseband SAFT in order to reduce the requirement for high-sampling rates associated with high-frequency systems.

ACKNOWLEDGMENTS

The authors also thank Y.-F. Chen and H. Kuo for assistance in acquiring the mouse ultrasound data. The authors also appreciate the helpful comments made by the reviewers.

REFERENCES

- [1] M. Berson, L. Vaillant, F. Patat, P. Vaillant, and L. Pourcelot, "High-resolution real-time ultrasonic scanner," *Ultrasound Med. Biol.*, vol. 18, no. 5, pp. 471–478, 1992.
- [2] G. R. Lockwood, D. H. Turnbull, D. A. Christopher, and F. S. Foster, "Beyond 30 MHz—Applications of high frequency ultrasound imaging," *IEEE Eng. Med. Biol. Mag.*, vol. 15, no. 6, pp. 60–71, 1996.
- [3] F. L. Lizzi, C. X. Deng, E. J. Feleppa, D. J. Coleman, and R. H. Silverman, "Three-dimensional biometric images of ocular structures using very-high-frequency ultrasound," in *Proc. IEEE Ultrason. Symp.*, 1999, pp. 1581–1583.
- [4] W. H. Chen, E. J. Gottlieb, J. M. Cannata, Y. F. Chen, and K. K. Shung, "Development of sector scanning ultrasonic backscatter microscope," in *Proc. IEEE Ultrason. Symp.*, 2000, pp. 1681–1684.
- [5] D. A. Knapik, B. Starkoski, C. J. Pavlin, and F. S. Foster, "A 100–200 MHz ultrasound biomicroscope," *IEEE Trans. Ultrason., Ferroelect., Freq. Contr.*, vol. 47, no. 6, pp. 1540–1549, 2000.
- [6] F. S. Foster, C. J. Pavlin, K. A. Harasiewicz, D. A. Christopher, and D. H. Turnbull, "Advances in ultrasound biomicroscopy," *Ultrasound Med. Biol.*, vol. 26, no. 1, pp. 1–27, 2000.
- [7] S. Erickson, D. Kruse, and K. Ferrara, "A hand-held, high frequency ultrasound scanner," in *Proc. IEEE Ultrason. Symp.*, 2001, pp. 1465–1468.
- [8] C. Passmann and H. Ermert, "In vivo imaging of the skin in the 100 MHz region using the synthetic aperture concept," in *Proc. IEEE Ultrason. Symp.*, 1995, pp. 1287–1290.
- [9] C. Passmann and H. Ermert, "A 100-MHz ultrasound imaging system for dermatologic and ophthalmologic diagnostics," *IEEE Trans. Ultrason., Ferroelect., Freq. Contr.*, vol. 43, no. 4, pp. 545–552, 1996.
- [10] G. H. Frazier and W. D. O'Brien, "Synthetic aperture technique with a virtual source element," *IEEE Trans. Ultrason., Ferroelect., Freq. Contr.*, vol. 45, no. 1, pp. 196–207, 1998.
- [11] M. Karaman, P.-C. Li, and M. O'Donnell, "Synthetic aperture imaging for small scale systems," *IEEE Trans. Ultrason., Ferroelect., Freq. Contr.*, vol. 42, no. 3, pp. 429–442, 1995.
- [12] S. Krishnan, K. W. Rigby, and M. O'Donnell, "Efficient parallel adaptive aberration correction," *IEEE Trans. Ultrason., Ferroelect., Freq. Contr.*, vol. 43, no. 1, pp. 691–703, 1998.
- [13] M. O'Donnell, "Efficient parallel receive beam forming for phased array imaging using phase rotation," in *Proc. IEEE Ultrason. Symp.*, 1990, pp. 1495–1498.
- [14] K. W. Rigby, "Method and apparatus for coherence filtering of ultrasound images," U.S. Patent 5 910 115, 1999.
- [15] K. W. Hollman, K. W. Rigby, and M. O'Donnell, "Coherence factor of speckle from a multi-row probe," in *Proc. IEEE Ultrason. Symp.*, 1999, pp. 1257–1260.
- [16] M.-L. Li and P.-C. Li, "A new adaptive imaging technique using generalized coherence factor," in *Proc. IEEE Ultrason. Symp.*, 2002, pp. 1627–1630.
- [17] P.-C. Li and M.-L. Li, "Adaptive imaging using the generalized coherence factor," *IEEE Trans. Ultrason., Ferroelect., Freq. Contr.*, vol. 50, no. 2, pp. 128–141, 2003.
- [18] M.-H. Bae and M.-K. Jeong, "A study of synthetic-aperture imaging with virtual source elements in B-mode ultrasound imaging systems," *IEEE Trans. Ultrason., Ferroelect., Freq. Contr.*, vol. 47, no. 6, pp. 1510–1519, 2000.
- [19] W. Masri, M. Mina, S. S. Udpa, L. Udpa, T. Xue, and W. Lord, "Synthetic aperture focusing techniques applied in the near field of a focused transducer," in *Proc. IEEE Ultrason. Symp.*, 1995, pp. 783–786.
- [20] T. Christopher, "Finite amplitude distortion-based inhomogeneous pulse echo ultrasonic imaging," *IEEE Trans. Ultrason., Ferroelect., Freq. Contr.*, vol. 44, no. 1, pp. 125–139, 1997.
- [21] T. Christopher, "Experimental investigation of finite amplitude distortion-based inhomogeneous pulse echo ultrasonic imaging," *IEEE Trans. Ultrason., Ferroelect., Freq. Contr.*, vol. 45, no. 1, pp. 158–162, 1998.
- [22] D. H. Simpson and P. N. Burns, "Pulse inversion Doppler: A new method for detecting nonlinear echoes from microbubble contrast agent," in *Proc. IEEE Ultrason. Symp.*, 1997, pp. 1597–1600.
- [23] D. H. Simpson, C. T. Chin, and P. N. Burns, "Pulse inversion Doppler: A new method for detecting nonlinear echoes from microbubble contrast agent," *IEEE Trans. Ultrason., Ferroelect., Freq. Contr.*, vol. 46, no. 2, pp. 372–382, 1999.
- [24] C.-C. Shen and P.-C. Li, "Harmonic leakage and image quality degradation in tissue harmonic imaging," *IEEE Trans. Ultrason., Ferroelect., Freq. Contr.*, vol. 48, no. 3, pp. 728–736, 2001.
- [25] E. Cherin, J. K. Poulsen, A. F. W. Van der Steen, and F. S. Foster, "Comparison of nonlinear and linear imaging techniques at high frequency," in *Proc. IEEE Ultrason. Symp.*, 2000, pp. 1639–1643.

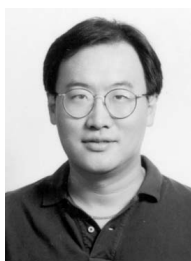


Meng-Lin Li (S'02) was born in 1976 in Tainan, Taiwan, R.O.C. He received the B.S. degree in electrical engineering from National Taiwan University, Taipei, Taiwan, R.O.C. in 1999. He is currently working toward the Ph.D. degree in electrical engineering at National Taiwan University. His current research interests include biomedical ultrasonic imaging, especially for synthetic aperture focusing and adaptive imaging, and signal processing. He is a student member of IEEE.



Wei-Jung Guan received the B.S. degree in Physics and the M.S. degree in Applied Physics from National Tsing-Hua University, Hsinchu, Taiwan, R.O.C., in 1998 and 2000, respectively. From 1997 to 2000, he was a research assistant in Microwave and Plasma Physics Laboratory with the Department of Physics at National Tsing-Hua University. From 2000 to 2002, he served as Artillery Reserved Officer with Armed Brigade in R.O.C. Army. From 2002 to 2003, he joined the Ultrasonic Imaging Laboratory, Department of

Electrical Engineering, National Taiwan University, as a research assistant. His work in the Ultrasonic Imaging Laboratory was to develop an *in vivo* high frequency ultrasound diagnostic system for biomedical research. He is currently working toward the Ph.D. degree in electrical engineering at Penn State University.



Pai-Chi Li (S'93–M'95–SM'01) received the B.S. degree in electrical engineering from National Taiwan University, Taipei, Taiwan, R.O.C., in 1987, and the M.S. and Ph.D. degrees from the University of Michigan, Ann Arbor, in 1990 and 1994, respectively, both in electrical engineering; systems.

He was a research assistant with the Department of Electrical Engineering and Computer Science at the University of Michigan from 1990 to 1994. He joined Acuson Corporation, Mountain View, CA, as a member of the technical staff in June 1994. His work in Acuson was primarily in the areas of medical ultrasonic imaging system design for both cardiology and general imaging applications. In August 1997, he went back to the Department of Electrical Engineering at National Taiwan University as an assistant professor. Then, he became an associate professor in August 1998. His current research interests include biomedical ultrasonic imaging and signal processing.

Dr. Li is a senior member of IEEE and Associate Editor of *IEEE Transactions on Ultrasonics, Ferroelectrics, and Frequency Control*. He received the 2002 Dr. Wu Dayou Research Award from the National Science Council, the 2002 Outstanding Young Electrical Engineer Award from the Chinese Institute of Electrical Engineering and the Distinguished Industrial Collaboration Award of Ministry of Education. He also was the recipient of the Distinguished Achievement Award in Electrical Engineering: Systems in 1994 for his outstanding academic achievement at the University of Michigan.